

# A Parallel Iterative Method for Computing Molecular Absorption Spectra

Peter Koval\*, Dietrich Foerster† and Olivier Coulaud‡

October 30, 2018

## Abstract

We describe a fast parallel iterative method for computing molecular absorption spectra within TDDFT linear response and using the LCAO method. We use a local basis of “dominant products” to parametrize the space of orbital products that occur in the LCAO approach. In this basis, the dynamical polarizability is computed iteratively within an appropriate Krylov subspace. The iterative procedure uses a matrix-free GMRES method to determine the (interacting) density response. The resulting code is about one order of magnitude faster than our previous full-matrix method. This acceleration makes the speed of our TDDFT code comparable with codes based on Casida’s equation. The implementation of our method uses hybrid MPI and OpenMP parallelization in which load balancing and memory access are optimized. To validate our approach and to establish benchmarks, we compute spectra of large molecules on various types of parallel machines.

The methods developed here are fairly general and we believe they will find useful applications in molecular physics/chemistry, even for problems that are beyond TDDFT, such as organic semiconductors, particularly in photovoltaics.

The manuscript is submitted to *Journal of Chemical Theory and Computation*, 28.05.2010.

## Contents

<b>1</b>	<b>Introduction</b>	<b>2</b>
<b>2</b>	<b>Brief review of linear response in TDDFT</b>	<b>3</b>
<b>3</b>	<b>Treatment of excited states within LCAO</b>	<b>4</b>
<b>4</b>	<b>An iterative method for the calculation of the dynamical polarizability</b>	<b>5</b>
4.1	The GMRES method for the iterative solution of a linear system of equations . . . . .	5
4.2	Fast application of the Kohn-Sham response matrix to vectors . . . . .	6
<b>5</b>	<b>Calculation of the interaction kernels</b>	<b>6</b>
5.1	The Hartree kernel . . . . .	7
5.2	The exchange–correlation kernel . . . . .	8
<b>6</b>	<b>Parallelization of the algorithm</b>	<b>9</b>
6.1	Multi-thread parallelization . . . . .	9
6.1.1	Building the basis of dominant products . . . . .	9
6.1.2	Construction of the interaction kernels . . . . .	10
6.1.3	Computation of the dynamical polarizability . . . . .	10
6.2	Hybrid MPI-thread parallelization . . . . .	10
6.2.1	Parallelization of the basis of dominant products . . . . .	11
6.2.2	Parallelization of the interaction kernels . . . . .	11
6.2.3	Parallelization of the iterative procedure . . . . .	11

\*koval.peter@gmail.com, CNRS, HiePACS project, LaBRI

†d.foerster@cpmoh.u-bordeaux1.fr, CPMOH, University of Bordeaux 1

‡olivier.coulaud@inria.fr, INRIA SUD OUEST, HiePACS project

<b>7</b>	<b>Results</b>	<b>11</b>
7.1	Fullerene C <sub>60</sub> . . . . .	11
7.2	Polythiophene chains (complexity of the method) . . . . .	12
7.3	Quality of the parallelization . . . . .	13
7.3.1	Multi-thread parallelization . . . . .	13
7.3.2	Hybrid MPI-thread parallelization . . . . .	14
7.4	Fullerene C <sub>60</sub> versus PCBM . . . . .	16
<b>8</b>	<b>Conclusion</b>	<b>18</b>

# 1 Introduction

The standard way to investigate the electronic structure of matter is by measuring its response to external electromagnetic fields. To describe the electronic response of molecules, one may use time-dependent density functional theory (TDDFT) [1]. TDDFT has been particularly successful in the calculation of absorption spectra of finite systems such as atoms, molecules and clusters [1, 2] and for such systems it remains the computationally cheapest *ab-initio* approach without any empirical parameters.

In the framework of TDDFT [3], time-dependent Kohn-Sham like equations replace the Kohn-Sham equations of the static density-functional theory (DFT). Although these equations can be applied to very general situations [4], we will restrict ourselves to the case where the external interaction with light is small. This condition is satisfied in most practical applications of spectroscopy and can be treated by the linear response approximation.

TDDFT focuses on the dependent electron density  $n(\mathbf{r}, t)$ . One assumes the existence of an artificial time dependent potential  $V_{\text{KS}}(\mathbf{r}, t)$  in which (equally artificial) non interacting reference electrons acquire exactly the same time dependent density  $n(\mathbf{r}, t)$  as the interacting electrons under study. The artificial time dependent potential  $V_{\text{KS}}(\mathbf{r}, t)$  is related to the true external potential  $V_{\text{ext}}(\mathbf{r}, t)$  by the following equation

$$V_{\text{KS}}(\mathbf{r}, t) = V_{\text{ext}}(\mathbf{r}, t) + V_{\text{H}}(\mathbf{r}, t) + V_{\text{xc}}(\mathbf{r}, t).$$

Here  $V_{\text{H}}(\mathbf{r}, t)$  is the Coulomb potential of the electronic density  $n(\mathbf{r}, t)$  and  $V_{\text{xc}}(\mathbf{r}, t)$  the exchange-correlation potential. The exchange-correlation potential absorbs all the non trivial dynamics and in practice it is usually taken from numerical studies of the interacting homogeneous electron gas.

The above time dependent extension of the Kohn-Sham equation was used by Gross *et al* [5] to find the dynamical linear response function  $\chi = \frac{\delta n(\mathbf{r}, t)}{\delta V_{\text{ext}}(\mathbf{r}', t')}$  of an interacting electron gas, a response function that expresses the change of the electron density  $\delta n(\mathbf{r}, t)$  upon an external perturbation  $\delta V_{\text{ext}}(\mathbf{r}', t')$ . From the change  $\delta n(\mathbf{r}, t)$  of the electron density one may calculate the polarization  $\delta \mathbf{P} = \int \delta n(\mathbf{r}, t) \mathbf{r} d^3r$  that is induced by an external field  $\delta V_{\text{ext}}(\mathbf{r}, t)$ . The imaginary part of its Fourier transform  $\delta \mathbf{P}(\omega)$  provides us with the absorption coefficient and the poles of its Fourier transform provide information on electronic transitions.

Most practical implementations of TDDFT in the regime of linear response are based on Casida's equations [6, 7]. Casida has derived a Hamiltonian in the space of particle-hole excitations, the eigenstates of which correspond to the poles of the interacting response function  $\chi(\mathbf{r}, \mathbf{r}', \omega)$ . Although Casida's approach has an enormous impact in chemistry [7], it is computationally demanding for large molecules. This is so because Casida's Hamiltonian acts in the space of particle-hole excitations, the number of which increases as the square of the number of atoms.

Alternatively, one may also solve TDDFT linear response by iterative methods. A first example of an iterative method for computing molecular spectra is the direct calculation of the density change  $\delta n(\mathbf{r}, \omega)$  in a modified Sternheimer approach [1, 7]. In this scheme one determines the variation of the Kohn-Sham orbitals  $\delta \psi(\mathbf{r}, t)$  due to an external potential without using any response functions. By contrast, use of the response functions allowed van Gisbergen *et al* [8, 9] to develop a self-consistent iterative procedure for the variation of the density  $\delta n(\mathbf{r}, t)$  without invoking the variation of the molecular orbitals. There exists also an iterative approach based on the density matrix [10, 11]. This approach is quite different from ours, but its excellent results, obtained with a plane-wave basis, serve as a useful test of our LCAO based method.

Over the last few years, the authors of the present paper developed and applied a new basis in the space of products that appear in the application of the LCAO method to excited states [12, 13, 14]. This methodological improvement allows for a simplified iterative approach for computing molecular spectra and the present paper describes this approach. We believe that the methods developed here will be useful in molecular physics, not only in the context of TDDFT, but also for systems such as large organic molecules that, because of their excitonic features, require methods beyond ordinary TDDFT.

This paper is organized as follows. In section 2, we briefly recall the TDDFT linear response equations. In section 3, we introduce a basis in the space of products of atomic orbitals. In section 4, we describe our iterative method of computing the polarizability and in section 5, we explain how the interaction kernels are computed. Section 6 describes

the parallelization of our iterative method in both multi-thread and multi-process modes. In section 7, we present results and benchmarks of the parallel implementation of our code. We conclude in section 8.

## 2 Brief review of linear response in TDDFT

To find the equations of TDDFT linear response, one starts from the time dependent extension of the Kohn-Sham equation that was already mentioned in the introduction and which we rewrite as follows

$$V_{\text{KS}}([n], \mathbf{r}, t) = V_{\text{ext}}([n], \mathbf{r}, t) + V_{\text{H}}([n], \mathbf{r}, t) + V_{\text{xc}}([n], \mathbf{r}, t).$$

The notation  $[n]$  indicates that the potentials  $V_{\text{KS}}$ ,  $V_{\text{H}}$  and  $V_{\text{xc}}$  in this equation depend on the distribution of electronic charge  $n(\mathbf{r}, t)$  in all of space and at all times. To find out how the terms of this equation respond to a small variation  $\delta n(\mathbf{r}, t)$  of the electron density, we take their variational derivative with respect to the electron density

$$\frac{\delta V_{\text{KS}}([n], \mathbf{r}, t)}{\delta n(\mathbf{r}', t')} = \frac{\delta V_{\text{ext}}([n], \mathbf{r}, t)}{\delta n(\mathbf{r}', t')} + \frac{\delta}{\delta n(\mathbf{r}', t')} [V_{\text{H}}([n], \mathbf{r}, t) + V_{\text{xc}}([n], \mathbf{r}, t)].$$

The important point to notice here is that  $\frac{\delta V_{\text{KS}}}{\delta n}$  and  $\frac{\delta V_{\text{ext}}}{\delta n}$  are inverses of  $\chi_0 = \frac{\delta n}{\delta V_{\text{KS}}}$  and  $\chi = \frac{\delta n}{\delta V_{\text{ext}}}$  that represent the response of the density of free and interacting electrons to, respectively, variations of the potentials  $V_{\text{KS}}$  and  $V_{\text{ext}}$ . As the response  $\chi_0$  of free electrons is known and since we wish to find the response  $\chi$  of interacting electrons, we rewrite the previous equation compactly as follows

$$\chi^{-1} = \chi_0^{-1} - f_{\text{Hxc}}. \quad (1)$$

Here an interaction kernel  $f_{\text{Hxc}} = \frac{\delta}{\delta n} [V_{\text{H}} + V_{\text{xc}}]$  is introduced. Equation (1) has the form of a Dyson equation that is familiar from many body perturbation theory [15].

To make use of equation (1), it remains to specify  $\chi_0$  and  $f_{\text{Hxc}}$ . The Kohn-Sham response function  $\chi_0$  can be computed in terms of orbitals and eigenenergies [1] as will be discussed later in this section (see equation (3) below). For the exchange-correlation potential  $V_{\text{xc}}([n], \mathbf{r}, t)$ , we use the adiabatic local density approximation (ALDA) that is local in both time and space,  $V_{\text{xc}}([n], \mathbf{r}, t) = V_{\text{xc}}(n(\mathbf{r}, t))$ , therefore the interaction kernel  $f_{\text{Hxc}}$  will not depend on frequency

$$f_{\text{Hxc}} = \frac{1}{|\mathbf{r} - \mathbf{r}'|} + \delta(\mathbf{r} - \mathbf{r}') \frac{dV_{\text{xc}}}{dn}.$$

In principle one could determine the interacting response function  $\chi(\mathbf{r}, t, \mathbf{r}', t')$  from equation (1), determine the variation of density  $\delta n(\mathbf{r}, t) = \int \chi(\mathbf{r}, t, \mathbf{r}', t') \delta V_{\text{ext}}(\mathbf{r}', t') d^3 r' dt'$  due to a variation of the external potential  $\delta V_{\text{ext}}$  and find the observable polarization  $\delta \mathbf{P} = \int \delta n(\mathbf{r}, t) \mathbf{r} d^3 r$ . To realize these operations in practice, we use a basis of localized functions to represent the space dependence of the functions  $\chi_0(\mathbf{r}, \mathbf{r}', \omega)$  and  $f_{\text{Hxc}}(\mathbf{r}, \mathbf{r}')$ .

In order to introduce such a basis into the Petersilka–Gossmann–Gross equation (1), we eliminate the inversions in this equation and transform to the frequency domain

$$\chi(\mathbf{r}, \mathbf{r}', \omega) = \chi_0(\mathbf{r}, \mathbf{r}', \omega) + \int d^3 r_1 d^3 r_2 \chi_0(\mathbf{r}, \mathbf{r}_1, \omega) f_{\text{Hxc}}(\mathbf{r}_1, \mathbf{r}_2) \chi(\mathbf{r}_2, \mathbf{r}', \omega). \quad (2)$$

The density response function of free electrons  $\chi_0(\mathbf{r}, \mathbf{r}', \omega)$  can be expressed [1] in terms of molecular Kohn-Sham orbitals as follows

$$\chi_0(\mathbf{r}, \mathbf{r}', \omega) = \sum_{E, F} (n_F - n_E) \frac{\psi_E(\mathbf{r}) \psi_F(\mathbf{r}) \psi_F(\mathbf{r}') \psi_E(\mathbf{r}')}{\omega - (E - F) + i\varepsilon}. \quad (3)$$

Here  $n_E$  and  $\psi_E(\mathbf{r})$  are occupation factors and Kohn-Sham eigenstates of eigenenergy  $E$ , and the constant  $\varepsilon$  regularizes the expression, giving rise to a Lorentzian shape of the resonances. The eigenenergies  $E$  and  $F$  are shifted in such a way that occupied and virtual states have, respectively, negative and positive energies. Only pairs  $E, F$  of opposite signs,  $E \cdot F < 0$ , contribute in the summation as is appropriate for transitions from occupied to empty states.

We express molecular orbitals  $\psi_E(\mathbf{r})$  as linear combinations of atomic orbitals (LCAO)

$$\psi_E(\mathbf{r}) = X_a^E f^a(\mathbf{r}), \quad (4)$$

where  $f^a(\mathbf{r})$  is an atomic orbital. The coefficients  $X_a^E$  are determined by diagonalizing the Kohn-Sham Hamiltonian that is the output of a prior DFT calculation and we assume these quantities to be available. For the convenience of the reader, we use Einstein's convention of summing over repeated indices.

### 3 Treatment of excited states within LCAO

The LCAO method was developed in the early days of quantum mechanics to express molecular orbitals as linear combinations of atomic orbitals. When inserting the LCAO ansatz (4) into equation (3) to describe the density response, one encounters products of localized functions  $f^a(\mathbf{r})f^b(\mathbf{r})$  — a set of quantities that are known to be linearly dependent.

There is an extensive literature [16, 17, 18, 19] on the linear dependence of products of atomic orbitals. Baerends uses an auxiliary basis of localized functions to represent the electronic density [19, 20]. His procedure of fitting densities by auxiliary functions is essential both for solving Casida’s equations and in van Gisbergen’s iterative approach.

In the alternative approach of Beebe and coauthors [16], one forms the overlaps of products  $\langle ab|a'b' \rangle$  to disentangle the linear dependence of the products  $f^a(\mathbf{r})f^b(\mathbf{r})$ . The difficulty with this approach is its lack of locality and the  $O(N^4)$  cost of the construction of the overlaps [21].

Our approach is applicable to numerically given atomic orbitals of finite support and, in the special case of products on coincident atoms, it resembles an earlier construction by Aryasetiawan and Gunnarsson in the muffin tin context [22]. We ensure locality by focusing on the products of atomic orbitals for each overlapping pair of atoms at a time [12, 13]. Because our construction is local in space, it requires only  $O(N)$  operations. Our procedure removes a substantial part of the linear dependence from the set of products  $\{f^a(\mathbf{r})f^b(\mathbf{r})\}$ . As a result, we find a vertex like identity for the original products in terms of certain “dominant products”  $F^\lambda(\mathbf{r})$

$$f^a(\mathbf{r})f^b(\mathbf{r}) \sim \sum_{\lambda > \lambda_{\min}} V_\lambda^{ab} F^\lambda(\mathbf{r}). \quad (5)$$

Here the notation  $V_\lambda^{ab}$  alludes to the fact that the vertex  $V_\lambda^{ab}$  was obtained from an eigenvalue problem for the pair of atoms that the orbitals  $a, b$  belong to. The condition  $\lambda > \lambda_{\min}$  says that the functions corresponding to the (very many) small eigenvalues were discarded. By construction, the vertex  $V_\lambda^{ab}$  is non zero only for a few orbitals  $a, b$  that refer to the same pair of atoms that  $\lambda$  belongs to and, therefore,  $V_\lambda^{ab}$  is a sparse object. Empirically, the error in the representation (5) vanishes exponentially fast [23] with the number of eigenvalues that are retained. The convergence is fully controlled by choosing the threshold for eigenvalues  $\lambda_{\min}$  and from now on we assume equality in relation (5).

We introduce matrix representations of the response functions  $\chi_0$  and  $\chi$  in the basis of the dominant products  $\{F^\mu(\mathbf{r})\}$  as follows

$$\chi_0(\mathbf{r}, \mathbf{r}', \omega) = \sum_{\mu\nu} F^\mu(\mathbf{r}) \chi_{\mu\nu}^0(\omega) F^\nu(\mathbf{r}'); \quad \chi(\mathbf{r}, \mathbf{r}', \omega) = \sum_{\mu\nu} F^\mu(\mathbf{r}) \chi_{\mu\nu}(\omega) F^\nu(\mathbf{r}'). \quad (6)$$

For the non interacting response  $\chi_{\mu\nu}^0(\omega)$ , one has an explicit expression

$$\chi_{\mu\nu}^0(\omega) = \sum_{abcd, E, F} (n_F - n_E) \frac{(X_a^E V_\mu^{ab} X_b^F)(X_c^F V_\nu^{cd} X_d^E)}{\omega - (E - F) + i\epsilon}, \quad (7)$$

which can be obtained by inserting the LCAO ansatz (4) and the vertex ansatz (5) into equation (3).

We insert the expansions (6) into the Dyson equation (2) and obtain the Petersilka-Gossmann-Gross equation in matrix form

$$\chi_{\mu\nu}(\omega) = \chi_{\mu\nu}^0(\omega) + \chi_{\mu\mu'}^0(\omega) f_{\text{Hxc}}^{\mu'\nu'}(\omega) \chi_{\nu'\nu}(\omega), \quad (8)$$

with the kernel  $f_{\text{Hxc}}^{\mu\nu}$  defined as

$$f_{\text{Hxc}}^{\mu\nu} = \int d^3r d^3r' F^\mu(\mathbf{r}) f_{\text{Hxc}}(\mathbf{r}, \mathbf{r}') F^\nu(\mathbf{r}'). \quad (9)$$

The calculation of this matrix will be discussed in section 5.

Since molecules are small compared to the wavelength of light, one may use the dipole approximation and define the polarizability tensor

$$P_{ik}(\omega) = \int d^3r d^3r' \mathbf{r}_i \mathbf{r}'_k \chi(\mathbf{r}, \mathbf{r}', \omega).$$

Moreover, using equation (8) we find an explicit expression for the interacting polarizability tensor  $P_{ik}(\omega)$  in terms of the known matrices  $\chi^0$  and  $f_{\text{Hxc}}$

$$P_{ik}(\omega) = d_i^\mu \left( \frac{1}{1 - \chi^0(\omega) f_{\text{Hxc}}} \right)_{\mu\nu} \chi_{\nu\nu'}^0(\omega) d_k^{\nu'}, \quad (10)$$

where the dipole moment has been introduced  $d_i^\mu = \int F^\mu(\mathbf{r}) \mathbf{r}_i d^3r$ . Our iterative procedure for computing molecular absorption spectra is based on equation (10). Below, we will omit Cartesian indices  $i$  and  $k$  because we compute tensor components  $P_{ik}(\omega)$  independently of each other.

## 4 An iterative method for the calculation of the dynamical polarizability

In equation (10) the polarizability  $P(\omega)$  is expressed as a certain *average* of the inverse of the matrix  $A_\mu^\nu \equiv \delta_\mu^\nu - \chi_{\mu\nu}^0(\omega) f_{\text{Hxc}}^{\nu\nu}$ . A direct inversion of the matrix  $A_\mu^\nu$  is straightforward at this point, but it is computationally expensive and of unnecessary (machine) precision. Fortunately, iterative methods are available that provide the desired result at much lower computational cost and with a sufficient precision.

In fact, we already used an iterative biorthogonal Lanczos method to create an approximate representation of the matrix  $A_\mu^\nu$ , which can be easily inverted within the Krylov subspace under consideration [13]. In this work, however, we use a simpler approach of better computational stability to compute the polarizability (10). First, we calculate an auxiliary vector  $X = A^{-1}\chi^0 d$  by solving a linear system of equations  $AX = \chi^0 d$  with an iterative method of the Krylov type. Second, we compute the dynamical polarizability as a scalar product  $P = d^\mu X_\mu$ . In this way we avoid the construction of the full and computationally expensive response matrix  $\chi_0$ . Below, we give details on this iterative procedure.

### 4.1 The GMRES method for the iterative solution of a linear system of equations

As we explained above, the polarizability  $P(\omega)$  can be computed separately for each frequency, by solving the system of linear equations

$$(1 - \chi^0(\omega) f_{\text{Hxc}}) X(\omega) = \chi^0(\omega) d, \quad (11)$$

and by computing the dynamical polarizability as a scalar product  $P(\omega) = d^\mu X_\mu(\omega)$ .

We apply a generalized minimal residual method (GMRES) [24, 25] to solve the linear system of equations (11), which is of the form  $AX = b$ . GMRES belongs to the Krylov-type methods [24, 26] that represent a large matrix  $A$  in an iteratively built up Krylov-type basis  $|0\rangle, |1\rangle \dots |i\rangle$ . The first vector  $|0\rangle$  in the basis is chosen equal to  $|b\rangle$ , while further vectors are computed recursively via  $|i\rangle = A|i-1\rangle$ . As the vectors  $|i\rangle = A^i|0\rangle$  are not mutually orthogonal, one may enforce their orthogonality by using the Gram-Schmidt method

$$|i\rangle = A|i-1\rangle - \sum_{j=0}^{i-1} |j\rangle \langle j|A|i-1\rangle. \quad (12)$$

The orthonormal basis built in this way is used in the GMRES method to approximately solve the linear system of equations  $A|X\rangle = |b\rangle$  by minimizing the residual  $|r\rangle = A|X\rangle - |b\rangle$  within the Krylov-type subspace (12). The minimization of the residual occurs when the equation  $\sum_j \langle i|A|j\rangle \langle j|x\rangle = \langle i|b\rangle$  is satisfied and this set of equations is of much smaller size than the original problem. When the solution in the Krylov subspace  $\langle i|x\rangle$  is found, then an approximate solution in the original space can be computed from  $|X\rangle = \sum_i |i\rangle \langle i|x\rangle$ .

A suitable stopping criterion is essential for our method and we tested several criteria in order to keep the number of iterations small and achieve a reliable result at the same time. The conventionally used criterion that  $\varepsilon_r = |r|/|b|$  should be small is unreliable when the tolerance threshold is comparatively large ( $\varepsilon_r \approx 1\%$ ). Therefore we suggest an alternative combined criterion.

A natural stopping criterion for an iterative solver of the linear system of equations  $AX = b$  is a condition on the relative error of the solution  $\varepsilon_X = |\Delta X|/|X|$ .

In our case, the quantity of interest is the dynamical polarizability  $P = \langle d|X\rangle$ , therefore it is meaningful to impose a limit on the relative error of the polarizability  $\varepsilon_P = |\Delta P|/|P|$ . Estimations of the errors  $\varepsilon_X$  and  $\varepsilon_P$  can be easily obtained because  $|\Delta X\rangle = A^{-1}|r\rangle$  and  $\Delta P = \langle d|A^{-1}|r\rangle$ . We estimate  $|\Delta X\rangle$  and  $\Delta P$  using a matrix norm [27],  $\Delta X \approx |A^{-1}| |r\rangle$  and  $\Delta P \approx |A^{-1}| \langle d|r\rangle$ . We used the Frobenius norm of the Krylov representation of the matrix  $A^{-1}$ ,  $|A^{-1}| \approx \sqrt{\sum_{ij} |\langle i|A^{-1}|j\rangle|^2}$  because  $A$  is a non Hermitian matrix.

Both errors  $\varepsilon_X$  and  $\varepsilon_P$  tend to zero in the limit  $X \rightarrow X_{\text{exact}}$ , but for a threshold in the range of a few percent they behave differently. The condition upon  $\varepsilon_P$  is better tailored to the problem and it saves unnecessary iterations in many cases. However, in a few cases, the condition upon  $\varepsilon_P$  fails, while the condition upon  $\varepsilon_X$  works. Therefore, we use a condition on  $\varepsilon_P$  in “quick and dirty” runs and a combined condition  $\varepsilon_P < \varepsilon_{\text{tolerance}}$  and  $\varepsilon_X < \varepsilon_{\text{tolerance}}$  for reliable results.

In general, iterative methods of the Krylov type involve only matrix–vector products  $A|z\rangle$ . For an explicitly given matrix  $A$ , the operation  $|z\rangle \rightarrow A|z\rangle$  requires  $O(N^2)$  operations. Therefore the whole iterative method will scale as  $O(N^2 N_{\text{iter}})$ , where  $N_{\text{iter}}$  is the number of iterations until convergence. This is better than direct methods when  $N_{\text{iter}} \ll N$ , because a matrix–matrix multiplication takes  $O(N^3)$  operations.

To avoid matrix multiplications, the application of the matrix  $A = 1 - \chi^0(\omega) f_{\text{Hxc}}$  to a vector  $|z\rangle$  is done sequentially by computing first  $|z'\rangle = f_{\text{Hxc}}|z\rangle$  and then  $A|z\rangle = |z\rangle - \chi^0(\omega)|z'\rangle$ . The kernel matrix  $f_{\text{Hxc}}$  is computed before the iterative procedure. Because it is frequency independent, it can be easily stored and reused. By contrast, the response matrix  $\chi^0(\omega)$  is frequency dependent and computationally expensive and its explicit construction should be avoided. Therefore, only matrix–vector products  $\chi^0(\omega)|z\rangle$  will be computed as explained below without ever calculating the full response matrix  $\chi^0(\omega)$ .

## 4.2 Fast application of the Kohn-Sham response matrix to vectors

In previous papers [13, 14], we have described an  $O(N^2)$  construction of the entire response function  $\chi_{\mu\nu}^0(\omega)$ , but the prefactor was large. Paradoxically, the Krylov method presented above allows for a much faster computation of the absorption spectrum, although the cost of matrix–vector products  $\chi^0(\omega)|z\rangle$  scales asymptotically as  $O(N^3)$  (see below).

Starting point of our construction of the matrix–vector product  $\chi^0(\omega)|z\rangle$  is the expression (7) for the Kohn-Sham response matrix in the basis of dominant products

$$\chi_{\mu\nu}^0(\omega)z^\nu = \sum_{abcd,E,F} (n_F - n_E) \frac{(X_a^E V_\mu^{ab} X_b^F)(X_c^F V_\nu^{cd} X_d^E)}{\omega - (E - F) + i\varepsilon} z^\nu.$$

To compute this matrix–vector product efficiently, we decompose its calculation into a sequence of multiplications that minimizes the number of arithmetical operations by exploiting the sparsity of the vertex  $V_\mu^{ab}$ . The sequence we chose is

$$\chi_{\mu\nu}^0 z^\nu \sim \sum_E X_a^E V_\mu^{ab} \sum_F X_b^F X_c^F \boxed{V_\nu^{cd} X_d^E} z^\nu$$

Figure 1: A sequence of operations to compute the matrix–vector product.  $\chi_{\mu\nu}^0 z^\nu$ .

graphically represented in figure 1. For clarity, the frequency dependent denominator is omitted. Boxes represent the products to be performed at different steps. The innermost box contains a frequency independent quantity, that is also used in the last step. An algebraic representation of the computational steps is given in table 1.

Step	Expression	Complexity	Memory	Details of the Complexity
1	$\alpha_\nu^{cE} = V_\nu^{cd} X_d^E$	$O(N^2)$	$O(N^2)$	$N_{occ} n_{orb}^2 N_{prod}$
2	$\beta^{cE} = \alpha_\nu^{cE} v^\nu$	$O(N^2)$	$O(N^2)$	$N_\omega N_{occ} n_{orb} N_{prod}$
3	$a^{FE} = X_c^F \beta^{cE}$	$O(N^3)$	$O(N^2)$	$N_\omega N_{occ} N_{virt} N_{orb}$
4	$\gamma_b^E = \sum_F X_b^F a^{FE}$	$O(N^3)$	$O(N^2)$	$N_\omega N_{occ} N_{virt} N_{orb}$
5	$n_\mu = \sum_E X_a^E V_\mu^{ab} \gamma_b^E$	$O(N^2)$	$O(N)$	$N_\omega N_{occ} n_{orb} N_{prod}$

Table 1: The complexity and memory requirements during the computation of the matrix–vector product  $\chi^0(\omega)z$ . There are steps in the sequence with  $O(N^2)$  and  $O(N^3)$  complexity, where  $N$  is the number of atoms.  $N_\omega$  denotes the number of frequencies for which the polarizability is computed, and the remaining symbols are explained in the text.

In the first stage of the algorithm, we compute an auxiliary object  $\alpha_\nu^{cE} \equiv V_\nu^{cd} X_d^E$ . The vertex  $V_\nu^{cd}$  is a sparse object by construction. Therefore, we will spend only  $N_{occ} n_{orb}^2 N_{prod}$  operations, where  $N_{occ}$  is the number of occupied orbitals,  $N_{prod}$  is the number of products and  $n_{orb}$  is the number of orbitals that belong to a pair of atoms. The auxiliary object  $\alpha_\nu^{cE}$  is sparse and frequency independent. Therefore we store  $\alpha_\nu^{cE}$  and reuse it in the 5-th step of the matrix–vector product. The product  $\beta^{cE} \equiv \alpha_\nu^{cE} v^\nu$  will cost  $N_{occ} n_{orb} N_{prod}$  operations because each product index  $\nu$  “communicates” with the atomic orbital index  $c$  in one or two atoms. The matrix  $\beta^{cE}$  will be full, therefore the product  $a^{FE} \equiv X_c^F \beta^{cE}$  will cost  $N_{occ} N_{virt} N_{orb}$  i.e. this step has  $O(N^3)$  complexity with  $N_{virt}$  the number of unoccupied (virtual) states. The next step  $\gamma_b^E \equiv \sum_F X_b^F a^{FE}$  also has  $O(N^3)$  complexity with the same operation count. Finally, the sum  $n_\mu \equiv \sum_E X_a^E V_\mu^{ab} \gamma_b^E$  takes only  $O(N^2)$  operations because the vertex  $V_\mu^{ab}$  is sparse. The sequence involves  $O(N^3)$  operations, but due to prefactors, the run time is dominated by the  $O(N^2)$  part of the sequence for molecules of up to a hundred atoms.

## 5 Calculation of the interaction kernels

In the adiabatic local-density approximation (ALDA), the interaction kernel

$$f_H + f_{xc} = \frac{\delta V_H}{\delta n} + \frac{\delta V_{xc}}{\delta n}$$

is a frequency-independent matrix. While the representation of the Hartree kernel is straightforward in our basis

$$f_H^{\mu\nu} = \iint d^3 r d^3 r' F^\mu(\mathbf{r}) \frac{1}{|\mathbf{r} - \mathbf{r}'|} F^\nu(\mathbf{r}'), \quad (13)$$

the exchange–correlation kernel is not known explicitly and must be approximated. The locality of the LDA potential  $V_{xc}(\mathbf{r}) = V_{xc}(n(\mathbf{r}))$  leads to a simple expression for the exchange–correlation kernel

$$f_{xc}^{\mu\nu} = \int d^3r F^\mu(\mathbf{r}) f_{xc}(\mathbf{r}) F^\nu(\mathbf{r}), \quad (14)$$

where  $f_{xc}(\mathbf{r})$  is a (non linear) function of the density  $n(\mathbf{r})$ . In this section, we describe how the Hartree and exchange–correlation kernels are constructed.

## 5.1 The Hartree kernel

The basis functions  $F^\mu(\mathbf{r})$  that appear in the interaction kernels (13) and (14) are built separately for each pair of atoms. They are either *local* or *bilocal* depending on whether the atoms of the pair coincide or not. While the local products are spherically symmetric functions, the bilocal products possess only axial symmetry. Because of their axial symmetry, the bilocal products have a particularly simple representation in a *rotated* coordinate system

$$F^\mu(\mathbf{r}) = \sum_{j=0}^{j_{\text{cutoff}}} F_j^\mu(r') Y_{jm}(\mathbf{R}\mathbf{r}'), \quad \mathbf{r}' = \mathbf{r} - \mathbf{c}, \quad (15)$$

where the rotation  $\mathbf{R}$  and the center  $\mathbf{c}$  depend on the atom pair. In the rotated frame, the  $Z$ -axis coincides with the line connecting the atoms in the pair. We use radial products  $F_j^\mu(r)$  that are given on a logarithmic grid. The local products have a simpler, LCAO-like representation

$$F^\mu(\mathbf{r}) = F^\mu(|\mathbf{r} - \mathbf{c}|) Y_{jm}(\mathbf{r} - \mathbf{c}), \quad (16)$$

where the centers  $\mathbf{c}$  coincide with the center of the atom.

Using the algebra of angular momentum, we can get rid of the rotations  $\mathbf{R}$  in the bilocal basis functions (15) and transform the kernel (13) into a sum over two center Coulomb integrals  $\text{Cb}(1, 2)$

$$\text{Cb}(1, 2) = \iint d^3r_1 d^3r_2 g_{l_1 m_1}(\mathbf{r}_1 - \mathbf{c}_1) |\mathbf{r}_1 - \mathbf{r}_2|^{-1} g_{l_2 m_2}(\mathbf{r}_2 - \mathbf{c}_2). \quad (17)$$

The elementary functions  $g_{lm}(\mathbf{r}) = g_l(r) Y_{lm}(\mathbf{r})$  have a radial-angular decomposition similar to local products (16). The Coulomb interaction (17) becomes local in momentum space

$$\text{Cb}(1, 2) = \int d^3p g_{l_1 m_1}(\mathbf{p}) p^{-2} e^{i\mathbf{p}(\mathbf{c}_1 - \mathbf{c}_2)} g_{l_2 m_2}(\mathbf{p}), \quad (18)$$

where the Fourier image of an orbital  $g_{lm}(\mathbf{p})$  conserves its spherical symmetry

$$g_{lm}(\mathbf{p}) = i g_l(p) Y_{lm}(\mathbf{p}). \quad (19)$$

The radial part  $g_l(p)$  is given by the Hankel transform of the original radial orbital in coordinate space

$$g_l(p) = \sqrt{\frac{2}{\pi}} \int_0^\infty g_l(r) j_l(pr) r^2 dr. \quad (20)$$

Inserting the expression (19) into equation (18), expanding the plane wave  $e^{i\mathbf{p}(\mathbf{c}_1 - \mathbf{c}_2)}$  in spherical harmonics and using the algebra of angular momentum, we can reduce the integration in momentum space to a one-dimensional integral

$$I_{l_1, l_2, l}(R) = \int_0^\infty g_{l_1}(p) j_l(pR) g_{l_2}(p) dp, \quad (21)$$

where  $R \equiv |\mathbf{c}_1 - \mathbf{c}_2|$ .

We distinguish two cases in treating this integral according to whether the orbitals  $g_{lm}(\mathbf{r})$  are overlapping or not. For overlapping orbitals, we compute the integral (21) numerically using Talman's fast Hankel transform [28]. For non overlapping orbitals, one can compute the integral (21) exactly using a multipole expansion. To derive this expansion, we replace the functions  $g_l(p)$  in the equation (21) by their Hankel transforms (20)

$$I_{l_1, l_2, l}(R) = \frac{2}{\pi} \int_0^\infty dr_1 g_{l_1}(r_1) r_1^2 \int_0^\infty dr_2 g_{l_2}(r_2) r_2^2 \int_0^\infty j_l(r_1) j_l(pR) j_l(r_2) dp. \quad (22)$$

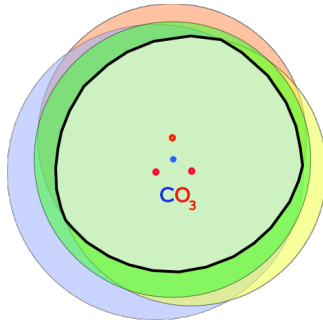


Figure 2: The spatial support of the integrand of the exchange correlation term (14) depends on the support of its underlying atomic orbitals and on the geometry of the quadruplet of atoms under consideration. For neighboring atoms, the support of the orbitals is several times larger than their inter atomic distances and this results in a nearly spherical support of the integrand. The figure illustrates the case of (hypothetical)  $\text{CO}_3$

The integral over three spherical Bessel functions  $I_{l_1, l_2, l}(r_1, r_2, R) \equiv \int_0^\infty j_{l_1}(r_1) j_l(pR) j_{l_2}(r_2) dp$  reduces to a simple separable expression [29] provided two conditions are satisfied,  $R > r_1 + r_2$  (the basis functions do not overlap), and  $0 \leq l \leq l_1 + l_2$  (the triangle relation for angular momentum). Under these conditions, we obtain

$$I_{l_1, l_2, l}(r_1, r_2, R) = \delta_{l, l_1 + l_2} \frac{\pi^{3/2}}{8} \frac{r_1^{l_1} r_2^{l_2}}{R^{l+1}} \frac{\Gamma(l+1/2)}{\Gamma(l_1+3/2)\Gamma(l_2+3/2)}. \quad (23)$$

Inserting this result into equation (22), we obtain an expression for the Coulomb interaction in terms of moments in closed form

$$\rho_l \equiv \int_0^\infty r^2 dr g_l(r) r^l. \quad (24)$$

The moments (24) can be computed and stored at the beginning of the calculation. Therefore, the calculation will consist of summing the angular-momentum coefficients and this is clearly much faster than a direct numerical integration in equation (21).

The complexity of the near-field interactions will be proportional to the number of atoms  $N$ . The calculation of the multipoles (24) for the far-field interaction requires of  $O(N)$  mathematical operations. The remaining part of the far-field interactions (Wigner rotations) scales as  $N^2$  with the number of atoms.

## 5.2 The exchange-correlation kernel

Unlike the Hartree kernel, the exchange-correlation kernel (14) is local and we therefore compute it directly in coordinate space by numerical quadrature. The support of the dominant products  $F^\mu(\mathbf{r})$ ,  $F^\nu(\mathbf{r})$  in the integrand of equation (14) have, in general, the shape of a lens. Therefore, the support of the integrand will generally be an intersection of two lenses.

We found, however, that integration in spherical coordinates gives sufficiently accurate and quickly convergent results. This is because the important matrix elements involve neighboring dominant products and the support of the dominant products is large compared to the distance between their centers. Therefore, the integrands of the important matrix elements (14) have nearly spherical support. This situation is illustrated by the cartoon in figure 2.

For each pair of dominant products, we use spherical coordinates that are centered at the midpoint between them. We use Gauss-Legendre quadrature for integrating along the radial coordinate and Lebedev quadrature [30] for integrating over solid angle

$$F_{xc} = \sum_{i=1}^{N_r} G_i \sum_{j=1}^{N_\Omega} L_j f_{xc}(r_i, \Omega_j). \quad (25)$$

Here  $G_i$  and  $r_i$  are weights and knots of Gauss-Legendre quadrature, and  $L_j$  and  $\Omega_j$  are weights and knots of Lebedev quadrature. The number of points  $N_r \times N_\Omega$  can be kept reasonably small ( $24 \times 170$  by default).

The most time consuming part of the exchange-correlation kernel is the electronic density. We found that calculating the density using the density matrix

$$n(\mathbf{r}) = \sum_{ab} f^a(\mathbf{r}) D_{ab} f^b(\mathbf{r}), \quad \text{where } D_{ab} = \sum_{E < 0} X_a^E X_b^E \quad (26)$$



provides a linear scaling of the run time of  $f_{xc}$  with the number of atoms. However, a calculation of the density via molecular orbitals

$$n(\mathbf{r}) = \sum_{E < 0} \psi_E(\mathbf{r})\psi_E(\mathbf{r}), \text{ where } \psi_E(\mathbf{r}) = \sum_a X_a^E f^a(\mathbf{r}) \quad (27)$$

is faster in many cases, although the run time scales quadratically with the number of atoms. In order to optimize the run time, rather than insist on linear scaling, we choose the calculational approach automatically depending on the geometry of the molecule. For instance, in the case of a long polythiophene with 13 chains (see subsection 7.2) we use the  $O(N)$  method, while in the other examples it is better to use the  $O(N^2)$  approach.

## 6 Parallelization of the algorithm

The overall structure of our algorithm is given in figure 3. First, the basis of dominant products is built, then the interaction kernels are computed, and finally both are used in the iterative procedure to compute the dynamical polarizability.

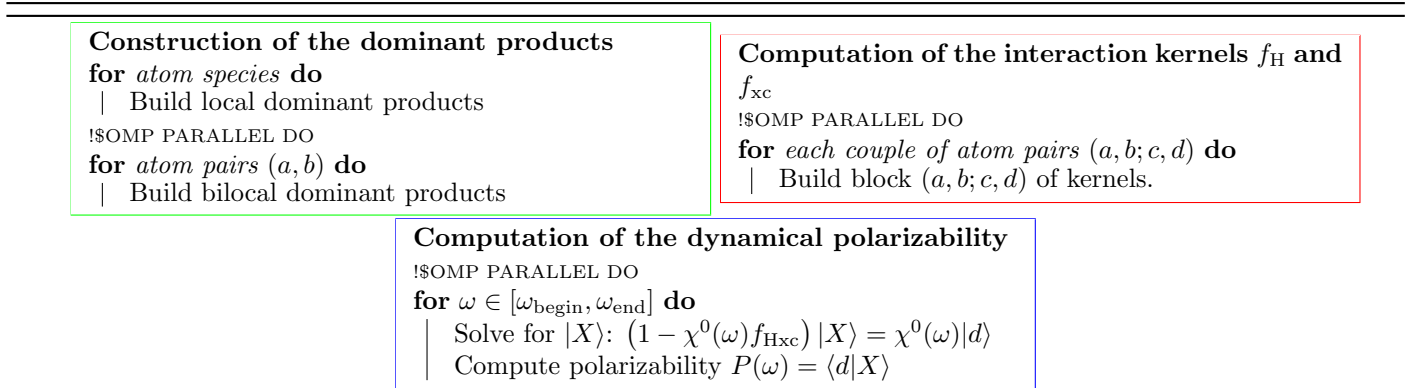


Figure 3: Skeleton of the algorithm. Its first (and computationally easiest) part is the construction of the dominant products. The second (and computationally most demanding) part is the construction of the interaction kernels. The third (and comparatively easy) part is the iterative calculation of the dynamical polarizabilities  $P(\omega)$ .

The individual components of the algorithm 3 suggest different parallelization strategies. The dominant products are built for each atom pair independently, therefore the corresponding code is parallelized over atom pairs. The structure of the dominant products suggests a block wise computation of the interaction kernels. These blocks are mutually independent, therefore we parallelize their construction. The dynamical polarizabilities are calculated independently for each frequency and are, therefore, parallelized over frequencies. Below, we go through the details of the algorithm and its hybrid OpenMP/MPI parallelization.

### 6.1 Multi-thread parallelization

Modern computers are faster than previous generations of machines mainly due to their parallel design as in the case of general-purpose multi-core processors. For specially written programs, such a design allows to run several tasks or “threads” simultaneously. Fortunately, it is easy to write a multi-threaded program using the current application programming interface OpenMP. Moreover, in OpenMP, data exchange between threads uses the common memory and it is, therefore, faster than on distributed-memory machines. For these reasons, our main emphasis here is on multi-threaded (or shared-memory) parallelization. We use the OpenMP standard [31] that allows for an efficient parallelization of all three sections of the algorithm 3.

#### 6.1.1 Building the basis of dominant products

The construction of local dominant products involves only the atomic species that occur in a molecule. Therefore it is computationally cheap and any parallelization would only slow down their construction.

For bilocal dominant products, the situation is different. The construction of bilocal dominant products is done for all atom pairs, the orbitals of which overlap. Because these pairs are independent of each other, we parallelize the loop over pairs with OpenMP directives.

The dominant products  $F^\mu(\mathbf{r})$  and vertices  $V_\mu^{ab}$  are stored in suitably chosen data structures to allow for effective use of memory. Due to the locality of our construction, the amount of memory spent in the storage of dominant products and vertices grows linearly with the number of atoms.

### 6.1.2 Construction of the interaction kernels

The interaction kernels (13) and (14) refer to a pair of dominant products  $F^\mu(\mathbf{r})$  and  $F^\nu(\mathbf{r})$ . Because each of the dominant products in turn refers to a pair of atoms, the interaction kernel splits into blocks that are labeled by a quadruplet of atoms  $(a, b; c, d)$ . In practice, this is used to precompute and reuse some auxiliary quantities that belong to such a quadruplet. The block structure is schematically depicted in figure 4. Generically, a block is rectangular, but when two pairs coincide, the block reduces to a triangle because of reflection symmetry.

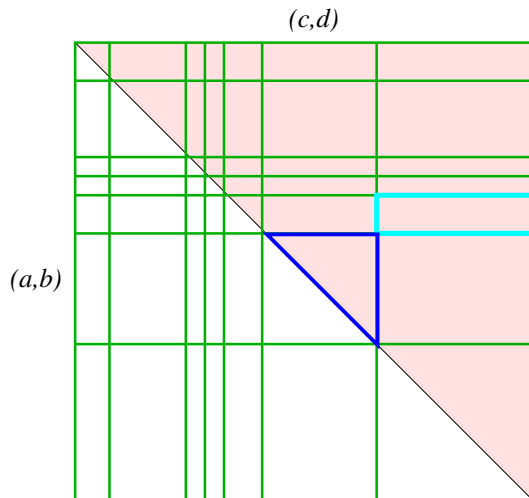


Figure 4: The block structure of the interaction kernels. The blocks are defined by two atom pairs  $(a, b)$  and  $(c, d)$ . The size of blocks is known from the construction of the dominant products. Because the entire interaction kernel  $f_{\text{Hxc}}^{\mu\nu}$  is symmetric, only its upper triangular part is computed.

The calculation of the interaction kernels is parallelized over blocks using dynamical scheduling. Because the computational load of each block is proportional to its area, we minimize the waiting time at the end of the loop by a descending sort of the blocks according to their area.

### 6.1.3 Computation of the dynamical polarizability

According to equation (10), the dynamical polarizability  $P_{ik}(\omega)$  is computed independently for each frequency  $\omega$ . Therefore, the loop over frequencies in the algorithm 3 is embarrassingly parallel.

In the parallelization over frequencies, we had to make thread safe copies of module variables (working arrays in the GMRES solver) using the OpenMP directive `threadprivate`. This multiplies the memory requirement by the number of threads, but this poses no problem, because this part of the algorithm is not memory intensive.

The number of iterations to reach convergence of the polarizability tensor (10) varies with frequency and with the Cartesian components in an irregular way. To take this into account, we use a dynamic schedule with a single frequency and tensor component per thread. By treating tensor components on the same level as frequencies, we reduce the body of a loop by a factor of three provided only diagonal components are computed.

## 6.2 Hybrid MPI-thread parallelization

Most current supercomputers are organized as clusters of multi-core nodes that are interconnected by a high speed network. Although the number of cores grows over the years, we still need several nodes for greater computational speed and to provide sufficient memory.

Our program has also been adapted to such distributed-memory parallel machines. We parallelize according to the Single Program Multiple Data (SPMD) paradigm with the message passing interface (MPI) to speed up only the computationally intensive parts of the algorithm — the construction of the bilocal products, the calculation of the kernels  $f_{\text{H}}$ ,  $f_{\text{xc}}$  and the iterative procedure. Moreover, each MPI process uses the multi-thread parallelism described above.

### 6.2.1 Parallelization of the basis of dominant products

Only bilocal dominant products must be constructed in parallel. As described in subsection 6.1.1, the construction is naturally parallel in terms of atom pairs. Therefore, we distribute the atom pairs prior to computation and gather data after the computation in order to duplicate basis functions on each MPI process.

### 6.2.2 Parallelization of the interaction kernels

As explained in subsection 6.1.2, the interaction kernel depends on quadruplets of atoms and it would appear natural to parallelize their construction over these quadruplets. We found it advantageous, however, to slice the interaction matrix into vertical bands that belong to one or more atom pairs and process them on different nodes. After the computation, the complete matrix of interactions is reconstituted on each node.

The optimal size of each vertical band is determined by an estimate of the work load prior to the computation. Since the Hartree and the exchange-correlation kernel differ in their properties (such as locality) their matrices are distributed differently. In both cases, however, the total work load is the sum of the work loads of its constituent quadruplets.

In the case of the Hartree kernel (13), the work load of a block depends on its size and on whether its atom pairs are local or bilocal. While the local products are of simple LCAO type (16), the bilocal products (15) contain additional summations. We found the following robust estimator of the workload of a block of the Hartree kernel

$$\text{Workload(Hartree)} = \text{Size\_Of\_Block} \cdot (j_{\text{cutoff}} \cdot \Theta(a \neq b) + 1) \cdot (j_{\text{cutoff}} \cdot \Theta(c \neq d) + 1), \quad (28)$$

where  $\Theta(a \neq b)$  is equal to one for bilocal atom pairs and zero otherwise,  $j_{\text{cutoff}}$  is the largest angular momentum in the expansion (15). By default, its upper limit is set to 7.

In the exchange-correlation kernel (14), the domain of integration is the intersection of two lens-like regions. Because there is no simple analytical expression for such a volume, we count the number of integration points within the support for each block and estimate the work load as proportional to the number of points. Rather surprisingly, the run time is independent of the dimension of the block (this is due to precomputing the values of the dominant products).

Because the kernel  $f_{\text{Hxc}}$  is frequency independent, it is computed at the beginning of the iterative procedure and duplicated on all the MPI-nodes. We found the time for gathering the matrix small compared to the time of its computation.

### 6.2.3 Parallelization of the iterative procedure

As mentioned previously in subsection 6.1.3, the iterative calculation of the polarizability tensor  $P_{ik}(\omega)$  is naturally parallel both in its frequency and in its Cartesian tensor indices. Therefore, this part of the algorithm is parallelized over both frequency and tensor indices. However, the workload for each composite index is difficult to predict. To achieve a balanced workload on the average, we distribute this index cyclically over MPI nodes (“round robin distribution”).

## 7 Results

In this section, we present different absorption spectra of large molecules to validate the method and the parallelization approach. We start in subsection 7.1 by comparing our absorption spectra with previous calculations by other authors and also with experimental data. Then, in subsection 7.2, we present the scaling of the run time with the number of atoms. In subsection 7.3, we examine the efficiency of the hybrid parallelization for a variety of molecules run on different machines. Finally, in subsection 7.4, we present a comparison of absorption spectra of fullerene  $\text{C}_{60}$  with its derivative PCBM that is often used in organic solar cells.

### 7.1 Fullerene $\text{C}_{60}$

We already tested the basis of dominant products in our previous works [12, 13, 14], where the absorption spectra of methane, benzene, indigo blue, and buckminsterfullerene  $\text{C}_{60}$  were studied. The new element in the present paper is the use of an iterative method without constructing the full Kohn-Sham response function. We now test this method on buckminster fullerene and its functionalized derivative PCBM.

Buckminster fullerene  $\text{C}_{60}$  is of considerable interest in materials science. Among other applications, it is used as an electron acceptor in organic solar cells [32]. Here we compare our results with spectra from the Quantum Espresso package and with experiment.

The absorption spectrum of fullerene  $\text{C}_{60}$  is shown in figure 5 where we compare our result with the calculation by Rocca *et al.* [10] and with experiment [33]. One can see a good agreement between the theoretical spectra, while both theoretical predictions deviate from the experimental data by 0.2...0.3 eV. The shift in the spectrum might be due to the solvent in the experimental setup or due to the inadequacy of the simplest LDA functional for this large molecule.

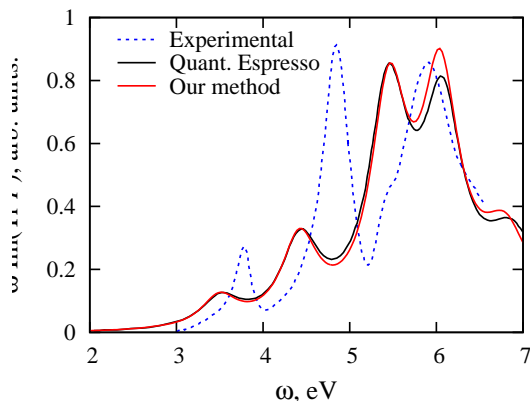


Figure 5: Comparison of the low-frequency absorption spectra of  $C_{60}$  fullerene. We see a good agreement between the two theoretical predictions, while the experimental curve is shifted by 0.2 . . . 0.3 eV.

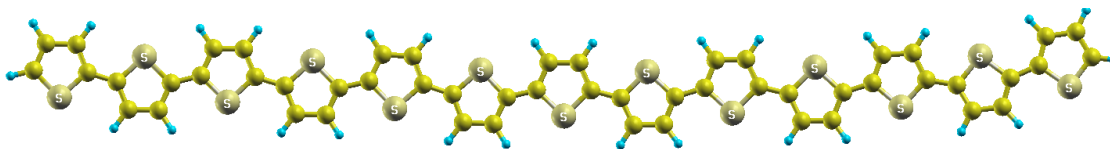


Figure 6: The geometry of the longest polythiophene chain we considered.

We used DFT data from the SIESTA package [34], where the pseudo-potentials of the Troullier-Martin type and the LDA functional by Perdew and Zunger [35] are applied. A double-zeta polarized basis set has been used and the broadening of levels has been set to 0.019 Ry. Our program spent a total of about 62.5 minutes on this calculation, of which 2098 seconds were spent on the Coulomb kernel, 1085 seconds on the exchange-correlation kernel, and 500 seconds in the iterative procedure, i. e. approximately 2.27 second per frequency. The convergence parameter for the polarizability was set to 1%. With this convergence parameter, the dimension of the Krylov space was varying from 7 to 12 with an average of 8, while the dimension of the dominant product space was 8700. In this test, we used one thread on a machine with two CPU Intel quad core Nehalem @ 2.93GHz; 8MB cache; 48GB DDR3 RAM, and consuming no more than 2.3% of RAM (1.2% during the iterative procedure).

## 7.2 Polythiophene chains (complexity of the method)

In sections 4 and 5, we discussed the complexity scaling of different parts of the algorithm theoretically. In this subsection, we measure the dependence of run time on the number of atoms  $N$  in polythiophene chains of different lengths. We shall see that the run time scaling follows the theoretical predictions for the complexity.

Sulfur containing molecules are widely use in organic electronics [32, 36, 37]. In this work, we study pure polythiophene chains of 3 to 13 repeating units. The geometry of the longest polythiophene we considered is shown in figure 6. Our calculations suggest (ignoring the excitonic character of these molecules) that the HOMO–LUMO energy difference decreases, while the absorption increases, with chain length. The calculated absorption spectra are collected in figure 7.

We now use the calculations on polythiophene spectra in order to study the run time scaling with the number of atoms of different parts of our algorithm. Their scaling behavior will be described in terms of approximate scaling exponents. The run times for a few chains are collected in table 2 for a machine of four CPU AMD Dual-Core Opteron @ 2.6GHz; 8MB cache; 32GB DDR2 RAM, and running sequentially.

The application of the non interacting response to a vector consists of  $N^2$ - and  $N^3$ -parts (see subsection 4.2). The total time for the product  $\chi^0 z$  is collected in the third column of table 2, while the run time of the  $N^3$ -part is collected in the fourth column. Using the run times, one can compute exponents  $x$  and  $x_3$  for their corresponding scaling laws  $N^x$  and  $N^{x_3}$ . The exponents  $x$  and  $x_3$  vary in the range of  $x = 2.31 \dots 2.36$  and  $x_3 = 2.49 \dots 2.53$ , respectively. The run time of the Hartree kernel (fifth column) shows a scaling exponent in the range  $x_H = 2.05 \dots 2.06$ , while the run time in the exchange–correlation kernel (sixth column) scales almost linearly  $x_{xc} = 1.04 \dots 1.12$ . Therefore, the measured exponents are close to the predicted exponents  $x = 3$ ,  $x_3 = 3$ ,  $x_H = 2$ , and  $x_{xc} = 1$ .

The calculation of the Hartree kernel  $f_H$  via multipoles, as explained in subsection 5.1 improves the run time in the case of large molecules, but could not improve the run time scaling of the Coulomb interaction. In fact, the Hartree kernel  $f_H$  is a non-local quantity and the rotations involved in the bilocal dominant products contribute a substantial part to

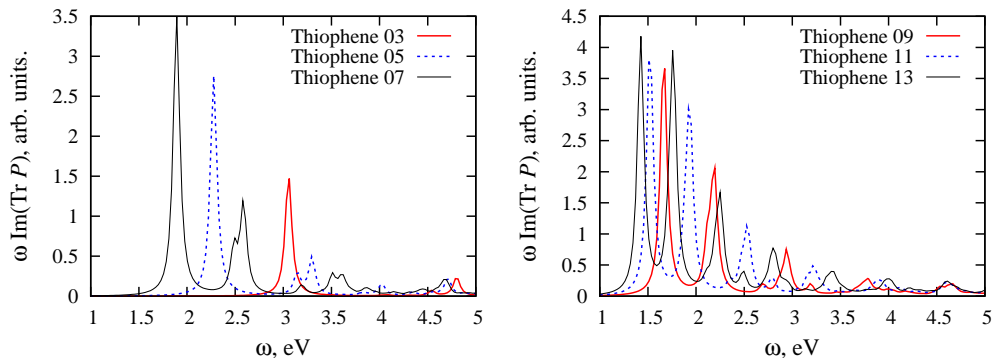


Figure 7: Comparison of low-frequency spectra for several polythiophene chains.

$N$	Units	$\chi^0 z$ , s	$N^3$ part in $\chi^0 z$ , s	$f_H$ , s	$f_{xc}$ , s
23	3	1.51E-02	8.20E-03	157	173
37	5	4.42E-02	2.52E-02	417	300
51	7	9.29E-02	5.58E-02	807	428
65	9	0.166	0.104	1324	561
79	11	0.260	0.169	1977	694
93	13	0.382	0.255	2767	822

Table 2: Run time in different parts of the algorithm as a function of the number of atoms  $N$  in the polythiophene chain. The third column gives the total time for the matrix–vector product ( $\chi^0 z$ ), while an  $N^3$ -part that arises in the construction of  $\chi^0 z$  is given in the fourth column. The fifth and sixth columns display the run times of the interaction kernels  $f_H$  and  $f_{xc}$ , respectively.

the run time.

The scaling of the run time for the entire calculation of molecular spectra will also vary with the parameters of the calculation. Obviously, for a small number of frequencies the scaling of total run time will be determined by the Hartree and exchange-correlation kernels. However, if the number of frequencies is large, then the application of the non interacting response  $\chi^0$  on a vector will dominate the run time.

### 7.3 Quality of the parallelization

Our parallel Fortran 90 code is adapted to current parallel architectures (see section 6). In this subsection, we evaluate the quality of the hybrid parallelization by testing our approach on three machines of different architecture. Two machines belong to shared-memory multi-core architectures with non uniform memory access, while the third machine is a cluster with 50 multi-core nodes interconnected by an Infiniband network.

The program was compiled using Intel’s Fortran compiler and linked against Intel’s Math Kernel Library for BLAS, LAPACK and Fast Fourier Transform libraries.

#### 7.3.1 Multi-thread parallelization

We consider parallelization on shared-memory machines as more important than on distributed-memory machines. Therefore, the speed up of our code is first tested on two shared-memory machines with Non-Uniform Memory Architecture (NUMA). The first machine has two quad core Nehalem 5500 CPUs (see figure 8), while the second machine has 48 dual core Xeon CPUs (see figure 10).

The speedup on the Nehalem machine is shown in figure 9 for three molecules of different size: benzene, indigo and fullerene. The speedup in both kernels and in the generation of bilocal products is good for all molecules, therefore we plot only the speedup for the Hartree kernel on the left panel. By contrast, the iterative procedure exhibits a lower speedup (as shown on the right panel in figure 9). This is due to the high memory-bandwidth requirement of the iterative procedure. The high memory-bandwidth is clearly revealed in two distinct ways of using the same number of cores in a test calculation, see subsection 7.3.2.

In spite of the loss of speed up for larger molecules on the Nehalem machine, we tested our implementation also on a parallel processor with a very large number of cores (see figure 10). The speedup is shown in figure 11.



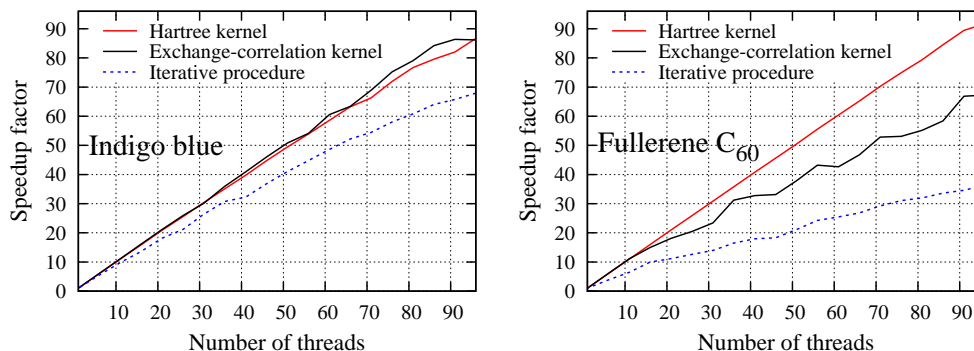


Figure 11: Speedup on a heavily parallel Xeon-96 machine. The results are satisfactory for the interaction kernels, while the memory-bandwidth requirements of the iterative procedure hamper the parallel performance in the case of the larger fullerene C<sub>60</sub> molecule.

Proc / Thr	Domi. prod.	$f_H$	$f_{xc}$	Iterative proc.	Total
1/8	7.3	271	142	145	571
2/4	6.9 (6.9)	273 (267)	142 (141)	109 (108)	538
4/2	6.8 (6.8)	274 (264)	142 (141)	122 (112)	544
8/1	6.8 (6.8)	274 (257)	143 (140)	134 (120)	570

Table 3: Run time and speedup factors in a hybrid MPI/OpenMP parallelization for fullerene C<sub>60</sub>. In the brackets, the smallest run time between the nodes is stated in order to estimate the MPI work load disbalance.

The high memory-bandwidth requirement is clearly revealed in two distinct ways of using the same number of cores (8 cores), either using all cores on one node or distributing them over two nodes. In the latter case, the memory-bandwidth is higher and the iterative procedure runs considerably faster (92 seconds versus 137 seconds in the case of fullerene C<sub>60</sub>).

We used the above optimal 2/4 hybrid configuration in a massively parallel calculation on the chlorophyll-a molecule. The speedup due to hybrid OpenMP–MPI parallelization is shown in figure 12. In this computation, we used up to 50 nodes of recent generation Nehalem machines. According to the previous experiment on fullerene C<sub>60</sub>, we started 2 processes per node, each process running with four threads. The two processes were placed on sockets. One can see that the iterative procedure shows the best speedup among other parts of the code, while total run time is governed mainly by the calculation of the exchange-correlation kernel. The absolute run times (including communication time) in the first calculation with one node (2 processes) were: total 4003 seconds, for the exchange-correlation kernel 1147 seconds, for the Hartree kernel 1247 seconds, for the iterative procedure 1574 seconds, and for the bilocal vertex 11.8 seconds. The speedup in the bilocal vertex reaches a maximum at 10 nodes because of increasing communication time.

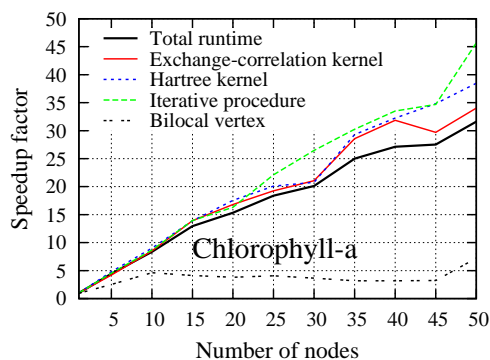


Figure 12: Speedup due to hybrid OpenMP/MPI parallelization for chlorophyll-a. The job was run on up to 50 nodes with 2 processes per node. The code shows a linear speedup on up to 15 nodes (30 processes, 120 cores). Further increase of the number of nodes results in a steady acceleration of the whole program.

The starting geometry of the molecule was taken from Sundholm’s supplementary data [38]. The geometry was further relaxed in the SIESTA package [34] using Broyden’s algorithm until the remaining force was less than 0.04 Ry/Å. The relaxed geometry is shown in figure 13. In order to achieve this (default) criterion, we had to use a finer internal mesh



with a `MeshCutoff` of 185 Ry. The default DZP basis was used, but to achieve convergence, we used orbitals that are more extended in space than SIESTA’s default orbitals. The spatial extension is governed by the parameter `PA0.EnergyShift` that was set to 0.002 Ry in the present calculation. The spectrum of the chlorophyll-a molecule is seen in figure 14. Like in the case of fullerene  $C_{60}$ , there is excellent agreements between theoretical results that however differ from the experimental data [39]. The low frequency spectrum consists of two bands at 635 nm and 450 nm. Both bands are due to transitions in the porphyrin. According to our calculation, the first A band consist of 2 transitions between HOMO–LUMO and HOMO-1–LUMO, while the second (so called Soret) band consist of 6 transitions to LUMO and LUMO+1 states.

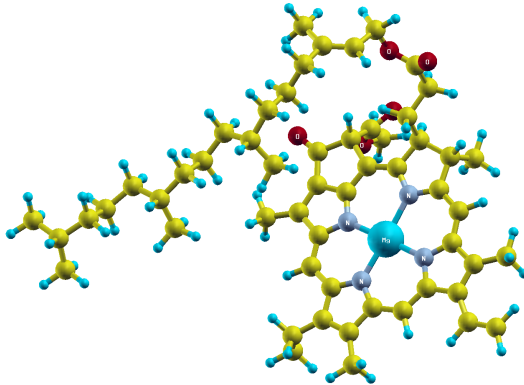


Figure 13: The relaxed geometry of chlorophyll-a molecule obtained with the SIESTA package using a DZP basis set.

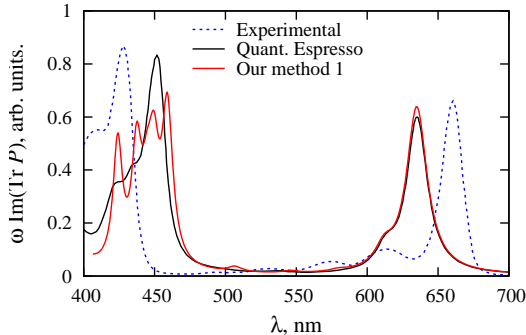


Figure 14: Low frequency absorption spectrum of chlorophyll-a.

## 7.4 Fullerene $C_{60}$ versus PCBM

Fullerenes are often modified in order to tune their absorption spectra or their transport properties [32, 40, 41]. In this work, we compute the absorption spectra of [6,6]-phenyl  $C_{61}$  butyric acid methyl ester (PCBM) and compare with the spectrum of pure fullerene  $C_{60}$ . We use the same parameters as in the case of  $C_{60}$  in subsection 7.1. A relaxed geometry of PCBM was obtained using the SIESTA package [34] and using its default convergence criterion (maximal force less than 0.04 eV/Å). Figure 15 shows the relaxed geometry. The absorption spectrum of PCBM is shown in figures 16 and 17.

Figure 16 shows a comparison of our calculation with recent experimental results [41]. We can see that our results have similar features as the experimental data: the maxima at 350 nm agree well with a broad experimental resonance at 355 nm, and a substantial “background” at longer wavelength is present both in the calculated and in the experimental spectrum. In this calculation, we set the damping constant  $\varepsilon = 0.08$  Ry and compute the spectrum in the range where experimental data are available. However, in order to better understand the difference introduced by the functional group, we compute the spectra in a broader range of energies with a smaller value of the damping constant  $\varepsilon = 0.003$  Ry. The result is shown in figure 17.

One can see on the left panel of figure 17 that PCBM absorbs much stronger in the visible range. This is a consequence of symmetry breaking and indicates a modified HOMO–LUMO gap. On the right panel of the figure, one can recognize the main difference between pure and modified fullerene. The high spatial symmetry of pure fullerene leads to a degeneracy



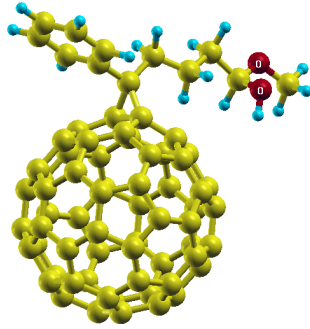


Figure 15: Geometry of PCBM. Relaxation is done in SIESTA package with Broyden's algorithm.

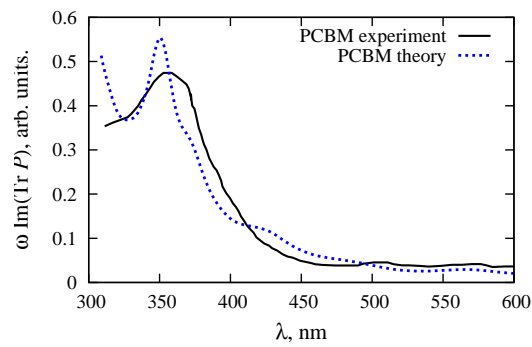


Figure 16: Comparison of the low-frequency spectra for PCBM with experimental data.

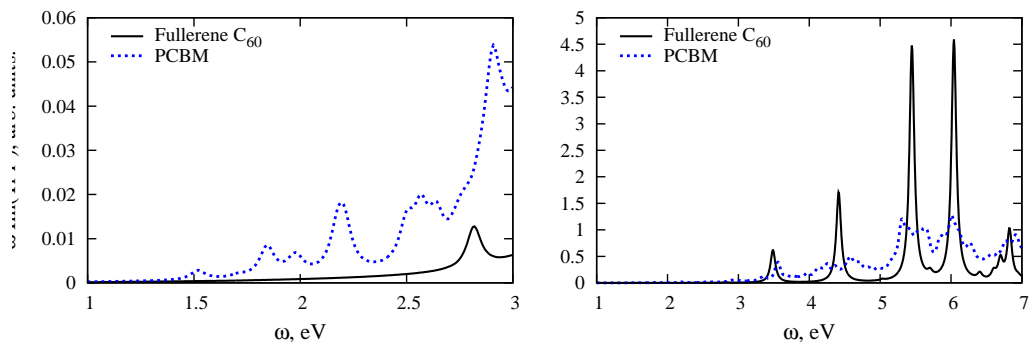


Figure 17: Comparison of the low-frequency spectra  $C_{60}$  versus PCBM.

of the electronic transitions and several transition contribute to the same resonance. The symmetry is broken in the case of PCBM, the degeneracy is lifted and the spectral weight is spread out.

## 8 Conclusion

In this paper, we have described a new iterative algorithm for computing molecular spectra. The method has two key ingredients. One is a previously constructed local basis in the space of products of atomic LCAO orbitals. The second is the computation of the density response not in the entire space of products, but in an appropriate Krylov subspace.

The speed of our code is roughly comparable to TDDFT codes in commercially available software but the reader must understand that we cannot give any details on this touchy issue.

The algorithm was parallelized and was shown to be suitable for treating molecules of more than hundred atoms on large current heterogeneous architectures using the OpenMP/MPI framework.

Our approach leaves plenty of room for further improvements both in the method and in the algorithm. For example, we did not consider reducing the dimension of the space in which the response function acts, but such a reduction is feasible.

Also, we chose a uniform mesh on the frequency axis while a more economical, adaptive choice is possible. We are working on an adaptive procedure to obtain good spectra with few frequency points and also to compute the position of the poles and strength of their residues. A reduction in the number of frequencies will allow to avoid the full calculation of the interaction kernels, replacing them by matrix-vector multiplications. There exist fast multipole methods [42] for computing fast matrix-vector products of the Hartree interaction.

Moreover, for large molecules, our embarrassingly parallel approach to compute spectra induces a memory-bandwidth bottleneck. To avoid it, one may parallelize the frequency loop using MPI and parallelize the matrix-vector operations using OpenMP.

More generally, because we do not use Casida’s equations, the methods developed here should be useful beyond the TDDFT approach, for instance in the context of Hedin’s GW approximation [43] where Casida’s approach is no longer available.

### Acknowledgement

We are indebted to Gustavo Scuseria for calling our attention to the existence of iterative methods in TDDFT and to Stan van Gisbergen for correspondence on the iterative method implemented in the Amsterdam Density Functional package (ADF).

It is our special pleasure to thank James Talman (University of Western Ontario, Canada) for contributing two crucial computer codes to this project. We thank Luc Giraud (HiePACS, Toulouse) for discussions on the GMRES algorithm and our colleagues Aurelian Esnard and Abdou Guermouch (University of Bordeaux) for technical advice.

We acknowledge useful correspondence on the SIESTA code by Daniel Sanchez-Portal (DIPC, San Sebastian) and also by Andrei Postnikov (Verlaine University, Metz). Advice by our colleagues of the ANR project CIS 2007 “NOSSI” especially Ross Brown and Isabelle Baraille (IPREM, Pau), is gratefully acknowledged. We also thank Uwe Huniak (Karlsruhe, Turbomole) for kindly supplying benchmarks of the TURBOMOLE package for comparison.

The results and benchmarks of this paper were obtained using the PlaFRIM experimental testbed of the INRIA PlaFRIM development project funded by LABRI, IMB, Conseil Régional d’Aquitaine, FeDER, Université de Bordeaux and CNRS (see <https://plafirim.bordeaux.inria.fr/>).

The work was done with financial support from the ANR CIS 2007 “NOSSI” project.

## References

- [1] *Time-Dependent Density Functional Theory*, edited by M. A. L. Marques, C. A. Ullrich, F. Nogueira, A. Rubio, K. Burke, E. K. U. Gross (Springer, Berlin, 2008).
- [2] *A Primer in Density Functional Theory*, edited by C. Fiolhais, F. Nogueira, M. A. L. Marques (Springer, Berlin, 2003).
- [3] E. Runge, E. K. U. Gross, Phys. Rev. Lett. **52**, 997 (1984).
- [4] M. A. L. Marques and E. K. U. Gross, Annu. Rev. Phys. Chem. **55**, 427 (2004);
- [5] M. Petersilka, U. J. Gossmann, and E. K. U. Gross, Phys. Rev. Lett., **76**, 1212 (1996).
- [6] M. E. Casida, in *Recent Advances in Density Functional Theory*, edited by D. P. Chong (World Scientific, Singapore, 1995), p. 155.

- [7] M. E. Casida, *J. Mol. Struct.: THEOCHEM* **914**, 3 (2009).
- [8] S. J. A. van Gisbergen, C. Fonseca Guerra, E. J. Baerends, *J. Comput. Chem.* **21**, 1511 (2000).
- [9] P.L. de Boeij, in *Time-Dependent Density Functional Theory*, edited by M. A. L. Marques, C. A. Ullrich, F. Nogueira, A. Rubio, K. Burke, E. K. U. Gross (Springer, Berlin, 2008).
- [10] D. Rocca, R. Gebauer, Y. Saad, and S. Baroni, *J. Chem. Phys.* **128**, 154105 (2008).
- [11] D. Rocca, *Time-dependent density functional perturbation theory*. PhD Thesis (Scuola Internazionale Superiore di Studi Avanzati, 2004)
- [12] D. Foerster, *J. Chem. Phys.* **128**, 034108 (2008).
- [13] D. Foerster, P. Koval, *J. Chem. Phys.* **131**, 044103 (2009).
- [14] P. Koval, D. Foerster, O. Coulaud, *Phys. Status Solidi B* **accepted** (2010).
- [15] A. L. Fetter, J. D. Walecka, *Quantum Theory of Many-Particle Systems* (McGraw-Hill, New York, 1971).
- [16] N. H. F. Beebe and J. Linderberg, *Int. J. Quantum Chem.* **7**, 683 (1977).
- [17] S. F. Boys, I. Shavitt., University of Wisconsin Naval Research Laboratory Report WIS-AF-13 (1959).
- [18] C.-K. Skylaris, L. Gagliardi, N. C. Handy, A. G. Ioannou, S. Spencer, A. Willetts, *J. Mol. Struct. THEOCHEM* **501–502**, 229 (2000).
- [19] E. J. Baerends, D. E. Ellis, P. Ros, *Chem. Phys.* **2**, 41 (1973).
- [20] G. Te Velde, F. M. Bickelhaupt, E. J. Baerends, C. Fonseca Guerra, S. J. A. van Gisbergen, J. G. Snijders, T. Ziegler, *J. Comput. Chem.* **22**, 931 (2001).
- [21] V. P. Vysotskiy and L. S. Cederbaum, **arXiv:0912.1459v1** (2009).
- [22] F. Aryasetiawan and O. Gunnarsson, *Phys. Rev. B* **49**, 16214 (1994).
- [23] U. Larrue, *Etude de la densité spectrale d'une métrique associée à l'équation de Schrödinger pour l'hydrogène*, unpublished (Bordeaux, 2008). This study showed an asymptotically uniform density of eigenvalues, on a logarithmic scale, for the metric in the case of the hydrogen atom.
- [24] Y. Saad, *Iterative Methods for Sparse Linear Systems* (Siam, Philadelphia 2003).
- [25] V. Frayssé, Luc Giraud, Serge Gratton, and Julien Langou, Algorithm 842: A set of GMRES routines for real and complex arithmetics on high performance computers. *ACM Trans. Math. Softw.* **31**, 228 (2005); <http://doi.acm.org/10.1145/1067967.1067970>.
- [26] I. C. F. Ipsen and C. D. Meyer, *The American Mathematical Monthly*, **105**, 889 (1998).
- [27] R. Barrett, M. W. Berry, T. F. Chan, J. Demmel, J. Donato, J. Dongarra, V. Eijkhout, R. Pozo, Ch. Romine, and H. van der Vorst, *Templates for the Solution of Linear Systems: Building Blocks for Iterative Methods* (Society of Industrial and Applied Mathematics, 1993).
- [28] J. D. Talman, *Comput. Phys. Commun.* **30**, 93 (1983); *Comput. Phys. Commun.* **180**, 332 (2009).
- [29] I. S. Gradshteyn and I. M. Ryzhik, *Tables of Integrals, Series and Products* (Academic Press, New York, 1980); formula 6.578/4.
- [30] V. I. Lebedev, *Russ. Acad. Sci. Dokl. Math.* **50**, 283 (1995). <http://www.ccl.net/ccl/software/SOURCES/FORTRAN/Lebedev-Laikov-Grids/>
- [31] <http://openmp.org/wp/>
- [32] Ch. J. Brabec, N. S. Sariciftci, and J. C. Hummelen, *Adv. Funct. Mater.* **11**, 15 (2001).
- [33] R. Bauernschmit, R. Ahlrichs, F. H. Hennrich, and M. M. Kappes, *J. Am. Chem. Soc.* **120**, 5052 (1998).

- [34] P. Ordejón, E. Artacho and J. M. Soler, Phys. Rev. **B 53**, R10441 (1996); J. M. Soler, E. Artacho, J. D. Gale, A. García, J. Junquera, P. Ordejón, D. Sánchez-Portal, J. Phys. **C 14**, 2745 (2002). We used different branches of SIESTA version 3 to perform calculations in this work.
- [35] J. P. Perdew, A. Zunger, Phys. Rev. **B 23**, 5048–5079 (1981).
- [36] F. Liang, J. Lu, J. Ding, R. Movileanu, and Ye Tao, Macromolecules **42**, 6107 (2009).
- [37] Y. Gao, Th. P. Martin, A. K. Thomas, and J. K. Grey, J. Phys. Chem. Lett. **1**, 178 (2010).
- [38] D. Sundholm, Chem. Phys. Lett. **302**, 480 (1999) <http://www.chem.helsinki.fi/~sundholm/qc/chlorophylla/>
- [39] H. Du, R. C. A. Fuh, J. Li, L. A. Corkan, and J. S. Lindsey, Photochem. Photobiol. **68**, 141 (1998); <http://omlc.ogi.edu/spectra/PhotochemCAD/html/index.html>.
- [40] A. C. Mayer, S. R. Scully, B. E. Hardin, M. W. Rowell, and M. D. McGehee, Materials today, **10**, 28 (2007).
- [41] P. Suresh, P. Balraju, G. D. Sharma, J. A. Mikroyannidis, and M. M. Stylianakis, ACS Appl. Mater. Interfaces, **1** 1370 (2009).
- [42] L. Greengard, V. Rokhlin, J. Comput. Phys. **73**, 325 (1987); L. Greengard, Science **265**, 909 (1994).
- [43] L. Hedin, S. Lundqvist, *Effects of Electron-Electron and Electron-Phonon Interactions on the One-Electron States of Solids*, in Solid State Physics, **23** (Academic Press, London, 1969).